

On the synthesis of acoustic sources with controllable near fields

D. Onofrei, E. Platt*

University of Houston, Department of Mathematics, United States



HIGHLIGHTS

- We present an optimization strategy for the synthesis of controllable fields.
- 3D control can be done exterior to the convex hull of the secondary sources.
- It's possible to have an incoming near field pattern with far field constraints.

ARTICLE INFO

Article history:

Received 23 June 2017
 Received in revised form 18 September 2017
 Accepted 18 October 2017
 Available online 2 November 2017

Keywords:

Acoustic control
 Inverse source problem
 Field synthesis
 Tikhonov regularization

ABSTRACT

In this paper we present a strategy for the synthesis of acoustic sources with controllable near fields in free space and constant depth homogeneous ocean environments. We first present the theoretical results at the basis of our discussion and then, to illustrate our findings we focus on the following three particular examples:

1. acoustic source approximating a prescribed field pattern in a given bounded sub-region of its near field.
2. acoustic source approximating different prescribed field patterns in given disjoint bounded near field sub-regions.
3. acoustic source approximating a prescribed *back-propagating* field in a given bounded near field sub-region while maintaining a very low far field signature.

For each of these three examples, we discuss the optimization scheme used to approximate their solutions and support our claims through relevant numerical simulations.

© 2017 Elsevier B.V. All rights reserved.

1. Introduction and main results

The problem of active control of acoustic fields is well studied in the literature with a multitude of ideas and techniques presented (see monographs [1,2]). The main strategies for active sound control are based on the use of boundary controls or secondary sources.

Applications of sound field control ideas are very important and they include: active noise control [3] (see also the pioneer works [4,5]), acoustic field reproduction [6–10] and active control of scattered sound fields [11–19]. A rigorous comparative analysis of the theoretical similarities and respective challenges for these three areas of applications is done in [20].

In a recent development in [21] (see also [22] for the low frequency approximation), a general analytical approach based on the theory of boundary layer potentials was proposed for the active acoustic control problem in homogeneous

* Corresponding author.

E-mail addresses: onofrei@math.uh.edu (D. Onofrei), eplatt@math.uh.edu (E. Platt).

environments. Then, in [23], building up on [21], the authors presented a thorough two dimensional sensitivity analysis for the synthesis of time-harmonic weak radiators with controllable patterns in some exterior region and, as indicated by their numerical results, postulated that such acoustic sources will be feasible only if the region of control is in the reactive near-field of the source.

The work presented in this paper uses ideas from, and is relevant to, a wide array of important research areas: acoustic wave field synthesis, inverse source problems, optimization, personal audio techniques, acoustic near field control. We are making use of the theoretical results developed in [21] and, through a Tikhonov regularization procedure (with Morozov discrepancy principle for the choice of the regularization parameter), we synthesize acoustic sources in one of the following scenarios:

1. Sources approximating a given pattern in a prescribed exterior near field sub-region.
2. Sources approximating a given pattern in a prescribed sub-region of their near field while giving a null in a different given sub-region of their near field.
3. Sources which have a very weak field in a given (sufficiently far) exterior annuli while approximating a given pattern in a prescribed sub-region of their near field.

The first type of sources are relevant for the problem of acoustic rendering [24,6]. The second type of sources above present an interest for the problem of personal audio studied in [8–11] where we assume that by superposition our strategy will imply the possibility to approximate, with such sources, different given sound patterns in disjoint regions of space. For the third type of sources above, although our theoretical results apply to the general question of synthesis of weak acoustic radiators approximating any given pattern in the near field control region, we focused on the problem of characterizing the necessary inputs (normal velocity or pressure) on the boundary of the source so that it approximates a backward propagating plane wave in the region of control while maintaining a very weak field in the given exterior annuli. This problem is relevant for the question of acoustic shielding or cloaking since by using a similar strategy we believe we can synthesize a planar array with similar properties: having a very weak field in an exterior annuli (where enemy detection measurements are taken) while approximating a given backward propagating plane wave in a near field region in front of it. Thus, by superposition, such an array could, when paired with a time control loop for the detection of interrogating signals, annihilate through destructive interference any incoming signal in its near field region without a large signature in its far field (i.e., shielding an object located behind the array). Then, a compact volume surrounded by a similar conformal array would lead to an active cloaking device for any object located inside.

The results presented in the literature regarding pattern synthesis use arrays of secondary sources (usually approximated by point sources) to control the field in interior regions (i.e., located in the interior of the geometric convex hull of the point sources), or focus on planar rendering (i.e. control in a horizontal plane) or assume that the field to be approximated propagate away from the source to be synthesized.

In the present paper we propose a theoretical optimization strategy for the synthesis of acoustic sources which approximate different prescribed field patterns in given disjoint *exterior* regions in free space and constant depth homogeneous ocean environments. To simplify the exposition, in the numerical support section, Section 3, we consider only the case of sources in free space and focus on the three particular cases listed above.

The paper is organized as follows: In Section 2 we present the theoretical results in two parts: first, in Section 2.1 we briefly recall the theoretical results of [21] for acoustic control in free space and then, in Section 2.2 we discuss their extension to the problem of underwater acoustic control in the context of a constant depth homogeneous ocean environments. In Section 3, we build up on our previous results in [23] and discuss the L^2 - Tikhonov regularization with Morozov discrepancy numerical approximation for the acoustic control problem in 3D and (assuming the superposition principle) without losing the generality present numerical simulations in the three important situations listed above: first, in Section 3.1 we present the synthesis of an acoustic source approximating a prescribed plane wave in a given near field sub-region; then in Section 3.2 we present the synthesis of an acoustic source with a null in a given sub-region of its near field and approximating an outgoing plane wave in a disjoint near field sub-region; and finally, in Section 3.3 we synthesize a very weak acoustic radiator (almost non-radiating source (ANR)) approximating, in a sub-region of its near field, a given backward propagating (propagating towards the source) plane wave. Finally, in Section 4 we present the conclusions of the paper with particular highlights for several possible applications of this work together with important future challenges.

2. Theoretical results

In this section we present the theoretical results behind our optimization scheme described below. In Section 2.1 we will recall the results of [21] developed for the free space environments (i.e., homogeneous media with no boundaries and radiating condition at infinity) and then in Section 2.2 we will present their extension to the case of constant depth homogeneous ocean environments as introduced in [25,26] (i.e., infinite rectangular waveguide with constant depth along z direction, $z \in [h, 0]$ for some $h < 0$, and pressure release boundary at the water–air interface $z = 0$, total reflecting boundary at the ocean bottom interface $z = h$ together with radiation condition at infinity).

We consider the source support represented by D_a , a compact region of space with Lipschitz continuous boundary, and as in [21] we assume that $D_1 \in \mathbb{R}^3$ and $D_2 \in \mathbb{R}^3$, with $D_1 \cap D_2 = \emptyset$ and $\{D_1 \cup D_2\} \cap D_a = \emptyset$. We also assume that u_1 is a

solution of the Helmholtz equation in a neighbourhood of D_1 and without losing the generality focus only on the case when $u_2 = 0$. With these general hypotheses, in what follows the following three geometrical situations will be considered:

- (i) D_1 bounded, $D_2 = \emptyset$,
- (ii) D_1 bounded, D_2 bounded, (2.1)
- (iii) D_1 bounded, D_2 unbounded with $D_1 \in \mathbb{R}^3 \setminus D_2$.

At this point we mention that the theoretical results of [21] hold true for any finite number of mutually disjoint regions $D_i, i \in \{1, \dots, n\}$ satisfying $\{\cup_i D_i\} \cap D_a = \emptyset$ and n scalar acoustic fields u_i each satisfying the Helmholtz equation in a neighbourhood of D_i , respectively.

In the case of free space environments the main problem is to characterize boundary inputs (normal velocity or pressure) on the surface of the source D_a such that the acoustic field radiated by it has the property that it approximates u_1 in D_1 and $u_2 = 0$ in region D_2 respectively (the condition on D_2 is not needed in case (2.1)(i) above).

2.1. Acoustic control in free space

In this section we will recall the result obtained in [21] in the geometrical setting described at (2.1): A source approximating prescribed acoustic patterns u_1 and $u_2 = 0$ in two given disjoint exterior regions, D_1 and respectively D_2 . Mathematically this can be written as follows:

Problem 1.

Find normal velocity v_n (or pressure p_b) on the boundary of the antenna ∂D_a so that,

$$\begin{cases} \Delta u + k^2 u = 0 \text{ in } \mathbb{R}^3 \setminus \bar{D}_a, \\ \nabla u \cdot \mathbf{n} = v_n, \text{ (or } u = p_b) \text{ on } \partial D_a, \\ \left(\frac{\mathbf{x}}{|\mathbf{x}|}, \nabla u(\mathbf{x}) \right) - iku(\mathbf{x}) = o\left(\frac{1}{|\mathbf{x}|}\right), \text{ as } |\mathbf{x}| \rightarrow \infty \text{ uniformly for all } \frac{\mathbf{x}}{|\mathbf{x}|}, \end{cases} \tag{2.2}$$

(where Δ denotes the 3D Laplace operator, ∇ denotes the 3D gradient, $q = o(a)$ means $\lim_{a \rightarrow 0} q = 0$, ∂S denotes the boundary of the set $S \in \mathbb{R}^3$ and here \mathbf{n} denotes the exterior normal to ∂D_a) and the following approximations hold true,

$$u \approx u_1, \text{ in } D_1, \text{ and } u \approx 0, \text{ in } D_2, \tag{2.3}$$

where the approximation in (2.3) is in the sense of smooth norms (e.g., twice differentiable functions)

As a consequence of results in [21] we have that Problem 1 above can be answered in the affirmative in all the geometrical configurations described at (2.1). Indeed, if k is not a resonance (i.e., for all wave numbers k except a discrete set [21]) we have that there exists an infinite class of smooth functions w (i.e., infinitely differentiable) so that normal velocity v_n (or pressure p_b) given by,

$$v_n(\mathbf{x}) = \frac{-i}{\rho c k} \frac{\partial}{\partial \mathbf{n}_x} \int_{\partial D'_a} w(\mathbf{y}) \frac{\partial \Phi(\mathbf{x}, \mathbf{y})}{\partial \mathbf{n}_y} ds_y, \text{ for } \mathbf{x} \in \partial D_a, \tag{2.4}$$

$$p_b(\mathbf{x}) = \int_{\partial D'_a} w(\mathbf{y}) \frac{\partial \Phi(\mathbf{x}, \mathbf{y})}{\partial \mathbf{n}_y} ds_y, \text{ for } \mathbf{x} \in \partial D_a, \tag{2.5}$$

(where ρ denotes the density of the surrounding medium, $D'_a \in D_a$ is a fictitious compact smooth domain (i.e. with C^2 boundary), \mathbf{n}_y denotes the exterior normal to $\partial D'_a$ computed in $\mathbf{y} \in \partial D'_a$ and Φ is the free space fundamental solution of the Helmholtz equation), will generate the required acoustic field u satisfying (2.2) and (2.3).

Remark 2.1. An important remark is that the actual physical source surface ∂D_a encloses the fictitious set \bar{D}'_a and needs to be Lipschitz but otherwise it can have any shape as long as $0 < \text{dist}(\bar{D}'_a, \bar{D}_1 \cup D_2)$ (where dist here denotes the distance between the two sets, i.e., $(\inf_{\mathbf{x} \in D_s, \mathbf{y} \in D_1 \cup D_2} |\mathbf{x} - \mathbf{y}|$ with $|\cdot|$ denoting the euclidean norm).

Remark 2.2. Note also that the fact that D'_a is smooth with $D'_a \in D_a$ in (2.4) or (2.5) implies that the boundary input v_n or p_b is smooth on ∂D_a . Moreover, this permits us to assume minimal smoothness for the boundary of the actual physical source ∂D_a (i.e., just enough to have the exterior problem well posed and thus Lipschitz will suffice) which may be very important for some applications, such as field synthesis, shielding, and cloaking.

Remark 2.3. We also point out that the normal velocity v_n (or pressure p_b) defined at (2.4), (or (2.5)) generate a solution u of (2.2), (2.3) represented as a double layer potential defined by

$$u(\mathbf{x}) = \int_{\partial D'_a} w(\mathbf{y}) \frac{\partial \Phi(\mathbf{x}, \mathbf{y})}{\partial \mathbf{n}_y} ds_y, \text{ for } \mathbf{x} \in \mathbb{R}^3 \setminus \bar{D}_a,$$

but, it is elementary to see how the results of [21] can be extended to obtain solutions of (2.2), (2.3) represented as a linear combination over \mathbb{C} between double layer and single layer potentials. This last formalism of representing a solution is efficient when dealing with real wave numbers k (see [27] for example).

2.2. Acoustic control in homogeneous oceans of constant depth

For the case of constant depth homogeneous ocean environments we follow the approach in [25,26] and model the surrounding homogeneous media as an infinite rectangular wave-guide, with constant depth h , i.e. $z \in [h, 0]$ (where z denotes the vertical coordinate in a rectangular coordinate system and $h < 0$), and assume a pressure release condition at the water–air interface, i.e., zero pressure at $z = 0$, and total pressure reflection at the bottom ocean interface, zero normal pressure at $z = h$ interface.

Let $\mathbb{R}_h^3 = \{\mathbf{x} = (\tilde{\mathbf{x}}, z) \in \mathbb{R}^3, \tilde{\mathbf{x}} = (x_1, x_2) \in \mathbb{R}^2, h \leq z \leq 0\}$ and consider domains D_1, D_2 and functions u_1 and $u_2 = 0$ as in Section 2.1. Assuming cylindrical coordinates and using the same notations as in (2.2), (2.3) the problem can be formulated mathematically as follows:

Problem 2.

Find normal velocity v_n (or the pressure p_b) on the boundary of the source ∂D_a so that u , the solution of,

$$\begin{cases} \Delta u + k^2 u = 0 \text{ in } \mathbb{R}_h^3 \setminus \bar{D}_a, \\ \nabla u \cdot \mathbf{n} = v_n, \text{ (or } u = p_b \text{), on } \partial D_a, \\ u = 0 \text{ on } z = 0, \quad \frac{\partial u}{\partial z} = 0 \text{ on } z = h, \\ \text{Radiation condition at infinity uniformly when } |\tilde{\mathbf{x}}| \rightarrow \infty, \end{cases} \tag{2.6}$$

satisfies

$$u \approx u_1, \text{ in } D_1, \text{ and } u \approx 0, \text{ in } D_2, \tag{2.7}$$

where as above in Section 2.1 the condition on D_2 is not needed in the case when $D_2 = \emptyset$. We mention that, the radiation condition at infinity in problem (2.6) is understood as in [25,26], i.e., for the solution u represented in normal mode expansion

$$u(\tilde{\mathbf{x}}, z) = \sum_{n=0}^{\infty} \phi_n(z) \psi_n(\tilde{\mathbf{x}}), \text{ for } r = |\tilde{\mathbf{x}}| > R,$$

we have that

$$\phi_n = \sin[k(1 - a_n^2)^{\frac{1}{2}}z], \text{ with } a_n = \left[1 - \frac{(2n + 1)^2 \pi^2}{4k^2 h^2} \right]^{\frac{1}{2}}, \tag{2.8}$$

and each of the ψ_n satisfy the following radiation condition when $r \rightarrow \infty$

$$\lim_{r \rightarrow \infty} r^{\frac{1}{2}} \left(\frac{\partial \psi_n}{\partial r} - ika_n \psi_n \right) = 0,$$

uniformly for $\theta \in [0, 2\pi]$ where $\theta = \tan^{-1}(\frac{x_2}{x_1})$. Next, we will describe how the results in [21] can be extended for this case. Indeed, assuming that k is not a resonant frequency (see Remark 2.4 for a precise statement), we have that there exists an infinite class of smooth functions w (infinitely differentiable) so that normal velocity v_n (or pressure p_b) given by,

$$v_n(\mathbf{x}) = \frac{-i}{\rho c k} \frac{\partial}{\partial \mathbf{n}_x} \int_{\partial D'_a} w(\mathbf{y}) \frac{\partial G(\mathbf{x}, \mathbf{y})}{\partial \mathbf{n}_y} ds_y, \text{ for } \mathbf{x} \in \partial D_a, \tag{2.9}$$

$$p_b(\mathbf{x}) = \int_{\partial D'_a} w(\mathbf{y}) \frac{\partial G(\mathbf{x}, \mathbf{y})}{\partial \mathbf{n}_y} ds_y, \text{ for } \mathbf{x} \in \partial D_a, \tag{2.10}$$

(where ρ denotes the density of the surrounding media, $D'_a \Subset D_a$ is a smooth region, \mathbf{n}_y denotes the exterior normal to $\partial D'_a$ computed in $\mathbf{y} \in \partial D'_a$ and G is the Green's function associated to problem (2.6)), will generate the required acoustic field u satisfying (2.6) and (2.7). Indeed, it is observed in [26] that for $\mathbf{y} = (\zeta, \tilde{\mathbf{y}})$, with $\tilde{\mathbf{y}} = (y_1, y_2)$, the Green's function G associated to problem (2.6) is given by,

$$G(z, \zeta, |\tilde{\mathbf{x}} - \tilde{\mathbf{y}}|) = \Phi(\mathbf{x}, \mathbf{y}) + \Phi_1(z, \zeta, |\tilde{\mathbf{x}} - \tilde{\mathbf{y}}|),$$

where Φ is the fundamental free space solution of the Helmholtz equation and Φ_1 above is bounded and continuous at $z = \zeta$ and $\tilde{\mathbf{x}} = \tilde{\mathbf{y}}$. Based on these considerations one can conclude that the double layer and the single layer operators associated with the Green's function G have the same compactness properties and satisfy the same jump relations as the classical layer potentials associated to Φ (see [26]). Thus, by using this together with a few elementary technical adjustments it can be proved that the results presented in [21] will extend to this case, i.e., normal velocities (or pressures) given by (2.9) (or (2.10))

will generate acoustic fields described by double layer potentials associated to G and satisfying (2.6) and (2.7). Moreover, the observation that expressions (2.9) and (2.10) can be used in computations since the Green’s function G is computed explicitly in [26].

The following remark brings some clarifications regarding the assumption that k is not a resonance for the present case.

Remark 2.4. Similar restrictions on k as for the free space discussion will apply for problem (2.6) and (2.7). Moreover, it is known in the literature [26,28] that the Dirichlet and Neumann exterior problems for the case of constant depth homogeneous oceans modelled as above is well posed for all values of k except a discrete set of values accumulating at $+\infty$. Thus, an extra restriction in this case should be that k is not an element of this discrete set. As an observation, for the Dirichlet problem, it is shown in [28] that by considering certain geometrical assumptions on ∂D_a the exterior Dirichlet problem is well posed for all wave numbers k .

We mention that the statement of Remark 2.2 applies to the case of finite depth homogeneous oceans as well. The following remark is similar in spirit along with Remark 2.3 but is presented here for the sake of completeness.

Remark 2.5. The normal velocity v_n (or the pressure p_b) given at (2.9) (or (2.10)) generates a solution u of (2.6), (2.7) represented as a double layer potential defined by

$$u(\mathbf{x}) = \int_{\partial D_{a'}} w(\mathbf{y}) \frac{\partial G(\mathbf{x}, \mathbf{y})}{\partial \mathbf{n}_y} dS_y, \text{ for } \mathbf{x} \in \mathbb{R}^3 \setminus \bar{D}_a,$$

but, in a similar manner as above, the results of [21] could be easily extended to obtain solutions of (2.6), (2.7) represented as a linear combination over \mathbb{C} between double layer and single layer potentials (see [26] for example).

3. Optimization schemes and numerical simulations

In this section we describe the mathematical ideas behind the optimization scheme used towards the approximation of solutions to (2.2), (2.3) and respectively (2.6), (2.7).

The L^2 - optimization and sensitivity analysis for the 2D formulation of the problem (2.2), (2.3) in the case (2.1)(iii) (with $\{D_1 \cup D_2\} \cap D_a = \emptyset$ as above), was performed in [23] where it was numerically observed that a good approximation of a stable solution with minimal power budget is achieved in the reactive near field of the source, i.e., when D_1 in (2.2) is located very close to the source D_a .

Similarly as in the 2D case treated in [23], the 3D L^2 - optimization scheme for problem (2.2), (2.3) is based on Tikhonov regularization with Morozov discrepancy principle. In this context, as in [21,23] regularity results and the well posedness of the interior and exterior acoustic boundary value problem (recall that k was chosen to be non-resonant) imply that in order to achieve approximate smooth controls in D_1 and D_2 it will be sufficient to have approximate L^2 controls on the boundaries of two slightly larger sets, $W_1 \in \mathbb{R}^3$ and $W_2 \in \mathbb{R}^3$, i.e., with $D_1 \in W_1$ and $D_2 \in W_2$. From (2.4) and Remark 2.3 it follows that solutions of (2.2), (2.3) can be approximated by a linear combination of double and single layer potentials, i.e.

$$\mathcal{D}w_\alpha(\mathbf{x}) = \eta_1 \int_{\partial D_{a'}} w_\alpha(\mathbf{y}) \frac{\partial \Phi(\mathbf{x}, \mathbf{y})}{\partial \nu_y} dS_y + i\eta_2 \int_{\partial D_{a'}} w_\alpha(\mathbf{y}) \Phi(\mathbf{x}, \mathbf{y}) dS_y, \tag{3.11}$$

where $\eta_1, \eta_2 \in \mathbb{R}$ are fixed parameters and where w_α is the Tikhonov regularization solution, i.e., minimizer of the following discrepancy functional,

$$F(w) = \frac{1}{\|f\|_{L^2(\partial D_c)}^2} \|\mathcal{D}w - u_1\|_{L^2(\partial W_1)}^2 + \mu \|\mathcal{D}w\|_{L^2(\partial W_2)}^2 + \alpha \|w\|_{L^2(\partial D_{a'})}^2, \tag{3.12}$$

with the regularization parameter α chosen according to the Morozov Discrepancy principle (see [23] for a 2D implementation in the case (2.1)(iii) and [29,30] for the general theoretical discussion) and the weight μ above given by

$$\mu = \begin{cases} 0, & \text{if } D_2 = \emptyset, \\ 1, & \text{if } D_2 \text{ is bounded,} \\ \frac{1}{4\pi R^2}, & \text{if } D_2 = \mathbb{R}^3 \setminus B_R(\mathbf{0}), \end{cases} \tag{3.13}$$

with $B_R(\mathbf{0})$ denoting the ball centred on the origin with a radius R such that $D_a \cup D_1 \in B_R(\mathbf{0})$.

For the numerical simulations we make use of the spherical harmonic decomposition for w_α (the density of the layer potential operators used to represent the solution (3.11)) and through the method of moments and Tikhonov regularization we approximate a solution of the problem (2.2) and (2.3) in all the geometrical situations described above at (2.1). In this regard in all of the numerical simulations below we assumed 30 spherical harmonic orders (total of 961 spherical harmonics) in the spherical harmonic decomposition of w_α .

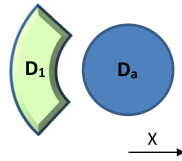


Fig. 1. Planar sketch of the geometry representing the source D_a and the region of control D_1 .

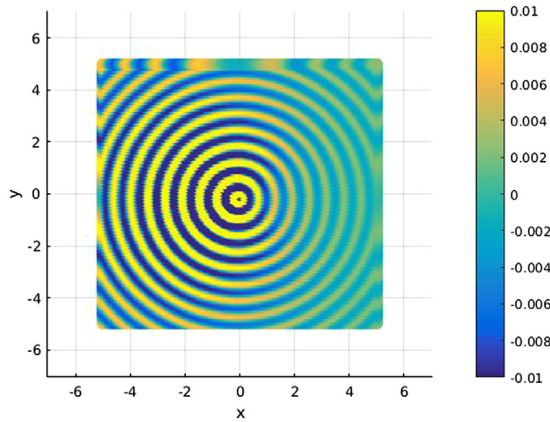


Fig. 2. Cross-section $z = 0$ plot of the generated field, showing outgoing character.

In all the simulations the fictitious domain D_a appearing in our strategy is the ball centred in the origin and radius 0.01 m and we use for its discretisation a total of 20,000 points, 200 equidistant azimuthal increments by 100 equidistant polar increments respectively. Also, for all the cases considered at (2.1) the left side control region D_1 is given by

$$D_1 = \{(r, \theta, \phi), r \in [0.011, 0.015], \theta \in [-\frac{\pi}{4}, \frac{\pi}{4}], \phi \in [\frac{3\pi}{4}, \frac{5\pi}{4}]\}. \tag{3.14}$$

(where r is measured in metres) and is represented in the numerical simulations by 6400 points, 40 equidistant azimuthal increments by 16 equidistant polar increments by 10 equidistant radial increments respectively.

We also note that in all the plots and animations presented the axis denote distances expressed in metres while the numbers marked on the colour bars represent actual values (and not dB). For dB translation one can always apply the $20\log_{10}$ convention to these actual values.

In the remainder of the paper we present numerical simulations of our strategy and, to simplify the exposition, we focus only on problem (2.2) and (2.3). Thus, the next three sections show our numerical simulations for the Tikhonov regularization solution corresponding to problem (2.2) and (2.3) as follows: Section 3.1 for the case (2.1)(i), Section 3.2 for the case (2.1)(ii) while Section 3.3 for the case (2.1)(iii).

3.1. Synthesis of a prescribed pattern in a subregion of the source near-field

In this section we present the Tikhonov regularization solution for the problem (2.2), (2.3) introduced in Section 2.1 describing the applications to the synthesis of acoustic sources approximating a given field patterns in a near field bounded region D_1 , see Fig. 1.

Thus, we will show the performance of the Tikhonov solution described in (3.11)–(3.13) in the case (2.1)(i). Without loss of generality we consider the case when the source to be synthesized approximates in region D_1 , described at (3.14), an outgoing plane wave propagating along the negative x -axis, $u_1 = e^{-ixk}$ with wave number $k = 10$.

First, in Fig. 2 we present a cross-sectional view of the generated field along $z = 0$ in a region characterized by $(x, y) \in [-5, 5]^2$. This plot indicates the synthesized source causality (i.e., the fact that the source field is outgoing), the generated field is outgoing satisfying the Sommerfeld radiation condition at infinity. This fact can also be observed in the time domain simulation presented in animation 1 [31] where the outgoing propagating time-harmonic field generated by the synthesized source is shown.

In Fig. 3 we present the quality of our control results in the region of interest D_1 as required in (2.3). The left and centre plots in the figure describe respectively the field generated by the source, and the plane wave to be approximated $u_1 = e^{-ixk}$ in region D_1 . The accuracy of our approximation $O(10^{-3})$ can be observed in the right picture of Fig. 3 where the relative

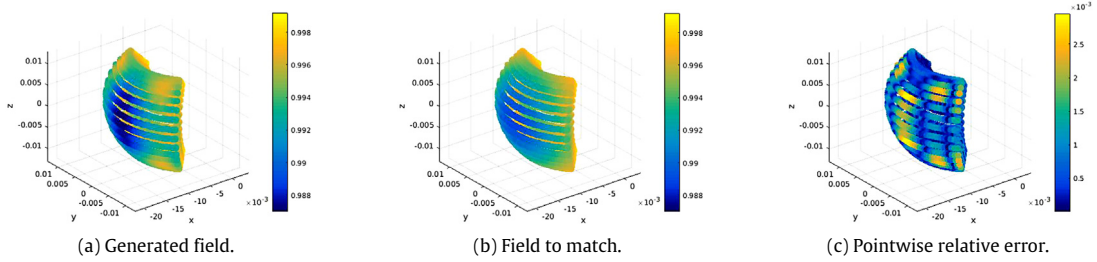


Fig. 3. Control accuracy in region D_1 .

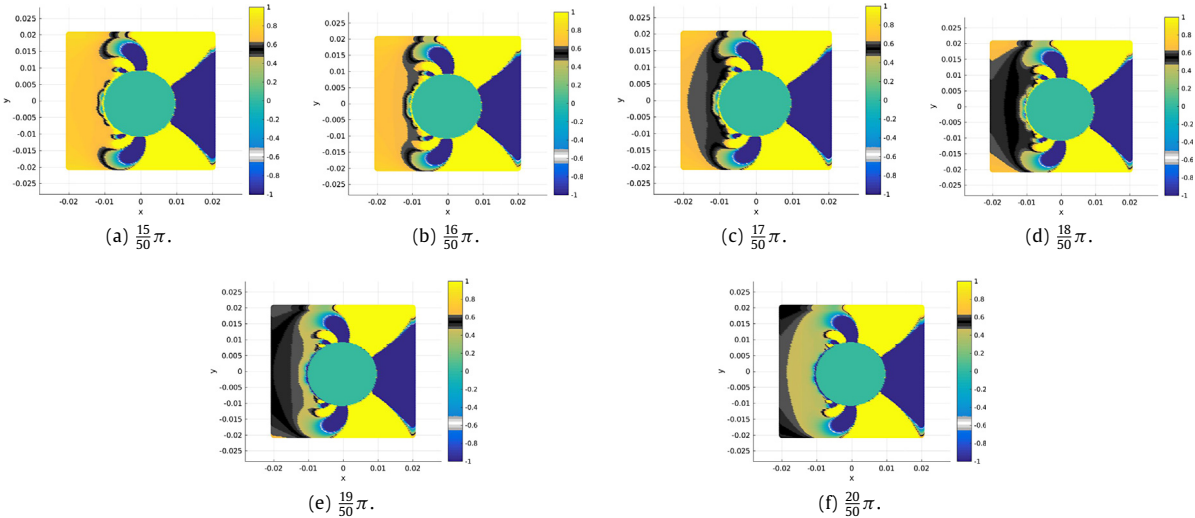


Fig. 4. Cross-sectional ($z = 0$) time snapshots of the propagating generated acoustic field for different values of kct . Control region D_1 to the left of the source. (For interpretation of the references to colour in this figure legend, the reader is referred to the web version of this article.)

pointwise error between u (the solution of (2.2)) and $u_1 = e^{-ixk}$ (the field to be approximated) is presented. Fig. 4 shows six cross-sectional views of the generated field along $z = 0$ in a near-field region characterized by $(x, y) \in [-0.02, 0.02]^2$. More explicitly, in order left to right from top left to bottom right plot, we present six cross-sectional ($z = 0$) time-snapshots (for $kct = \{\frac{15}{50}\pi, \frac{16}{50}\pi, \frac{17}{50}\pi, \frac{18}{50}\pi, \frac{19}{50}\pi, \frac{20}{50}\pi\}$) of the time-harmonic field generated by the synthesized source in the near field region, including the region of interest D_1 (where c here was used as the speed of sound in air). The colour scheme in the plots is (truncated to 1 light yellow and -1 dark blue) with the antenna region (coloured cyan) not included in the numerical simulations and with the black and white stripes representing field amplitudes approximately equal to 0.6 and -0.6 respectively. Following the plots in order (left to right) from top left to bottom right plot it can be observed how the source works to approximate an outgoing plane wave $u_1 = e^{-ixk}e^{-ikt}$ in region D_1 (e.g., corresponding rectilinear black stripe outgoing propagating through the control region). Indeed, the plots of Fig. 4 show the propagation of the generated field by focusing on the portion of the field with amplitude approximately equal to 0.6 marked as a dark stripe. It can be observed how this portion of the field enters region D_1 at time $kct = \frac{17}{50}\pi$ in a nearly rectilinear shape and continues to keep the same rectilinear form (indicating plane wave character of the approximated field in the control region) throughout the neighbourhood of region D_1 .

The time domain animation 2 [32] presents the cross-sectional view along $z = 0$ of the time-harmonic evolution of the field generated by the synthesized source and respectively the propagating plane wave $u_1 = e^{-ixk}e^{-ikt}$ in a near field region given by $(x, y) \in [-0.05, 0.05]^2$. The multimedia file shows two animations: the top one describing the time propagation of the generated field and the bottom one describing the time propagation of the plane wave $u_1 = e^{-ixk}e^{-ikt}$. The colour scheme in the movies is (truncated to 1 light yellow and -1 dark blue) with the region $D_{a'}$ removed from the simulations (coloured cyan) and with the black stripe representing amplitude values approximately equal to 0.6, and the white stripe representing amplitude values approximately equal to -0.6 respectively. Observing that there will be two black stripes and respectively two white stripes per period for the approximated plane wave one can see in the animation the accuracy of the approximation of the plane wave $u_1 = e^{-ixk}e^{-ikt}$ (rectilinear stripes) in region D_1 .

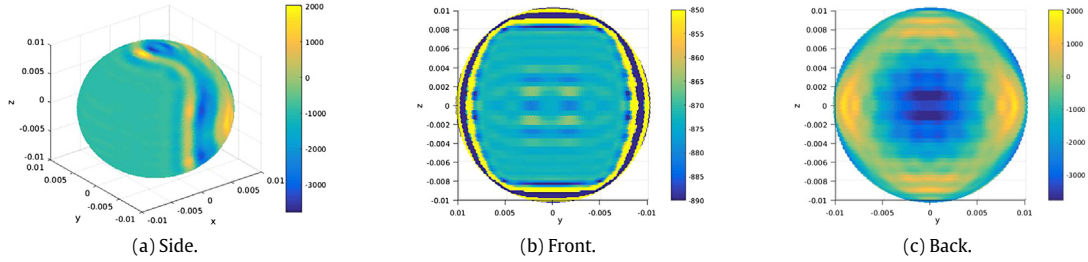


Fig. 5. Input density w_α with various colour maps highlighting the local oscillations.

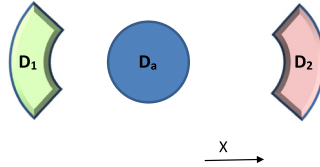


Fig. 6. Planar sketch of the geometry showing the source D_a , the control region D_1 and the null region D_2 .

Fig. 5 describes the density w_α (see (3.11)) on the boundary of the fictitious domain $D_{a'}$ (recall Remark 2.1 for the shape and location of the boundary of the actual physical source D_a) as an indication of the underlying complexity of the required source inputs v_n or p_b resulting from the present L^2 optimization procedure and described at (2.4) or (2.5). In the left plot of the figure we present the density values on the surface of $D_{a'}$ viewed in a side 3D perspective and for better visualization we show two more plots in the figure: the centre plot shows the density values on the part of the surface facing region D_1 while the right plot of the figure presents the density values on the opposite part of the surface.

3.2. Synthesis of different prescribed patterns in disjoint subregions of the source near-field

In this section we present the Tikhonov regularization solution for the problem (2.2), (2.3) described in Section 2.1 describing the applications to the synthesis of acoustic sources approximating two different field patterns in two prescribed disjoint near field regions. Thus, we show next the performance of the Tikhonov solution described in (3.11)–(3.13) in the case (2.1)(ii).

As in Section 3.1, we consider the case when the synthesized source approximates in region D_1 , described at (3.14), an outgoing plane wave propagating along the negative x_1 -axis, $u_1 = e^{-ixk}$ with wave number $k = 10$ while having a null in region $D_2 = \{(r, \theta, \phi), r \in [0.011, 0.015], \theta \in [-\frac{\pi}{4}, \frac{\pi}{4}], \phi \in [-\frac{\pi}{4}, \frac{\pi}{4}]\} + (0.018, 0, 0)$, (i.e. region D_2 is the same as region D_1 but shifted to the right along x_1 axis 0.018 units). We mention that, similar as for region D_1 , in the simulations presented in this section the control set D_2 is discretized with 6400 points, 40 equidistant azimuthal increments by 16 equidistant polar increments by 10 equidistant radial increments respectively. A sketch of the geometries are shown in Fig. 6. In Fig. 7 we present a cross-sectional view of the generated field along $z = 0$ in a region characterized by $(x, y) \in [-5, 5]^2$. As above, this plot supports the claim about the source causality (i.e., the fact that the source field is outgoing). This fact can be better observed in the time domain simulation presented in animation 3 [33] where the propagating time-harmonic field generated by the synthesized source is shown.

In Fig. 8 we present the quality of our control results in the two regions of interest D_1, D_2 as required in (2.3). The left and centre plots on the top row in the figure describe respectively the field generated by the source, and the outgoing plane wave to be approximated $u_1 = e^{-ixk}$. The accuracy of our approximation $O(10^{-3})$ can be observed in the right picture on the top row of Fig. 8 where the relative pointwise error between u (the field generated solution of (2.2)) and $u_1 = e^{-ixk}$ (the field to be approximated) is presented. The fourth picture in Fig. 8 (bottom row of the figure) presents a scattered plot with the values of the generated field in region D_2 where very small values of the field (associated with the null effect as required from the optimization procedure) can be observed.

Fig. 9, shows six cross-sectional views of the generated field along $z = 0$ in a near-field region characterized by $(x, y) \in [-0.05, 0.05]^2$. More explicitly, in order left to right and from top left to bottom right plot, we present six cross-sectional ($z = 0$) time-snapshots ($kct = \{\frac{83}{50}\pi, \frac{84}{50}\pi, \frac{85}{50}\pi, \frac{86}{50}\pi, \frac{87}{50}\pi, \frac{88}{50}\pi\}$) of the time-harmonic field generated by the synthesized source in the near field region, including the two regions of interest D_1, D_2 . The colour scheme in the plots is (truncated to 1 light yellow and -1 dark blue) with the antenna region not included in the numerical simulations and thus corresponding to zero values field (cyan colour) and with the black stripe and white strip representing field amplitudes approximately equal to 0.6 and -0.6 respectively. Following the plots in order left to right and from top left to bottom

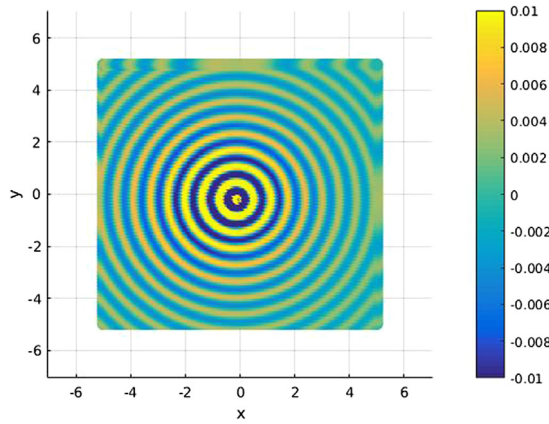


Fig. 7. Cross-section $z = 0$ plot of the generated field, showing outgoing character.

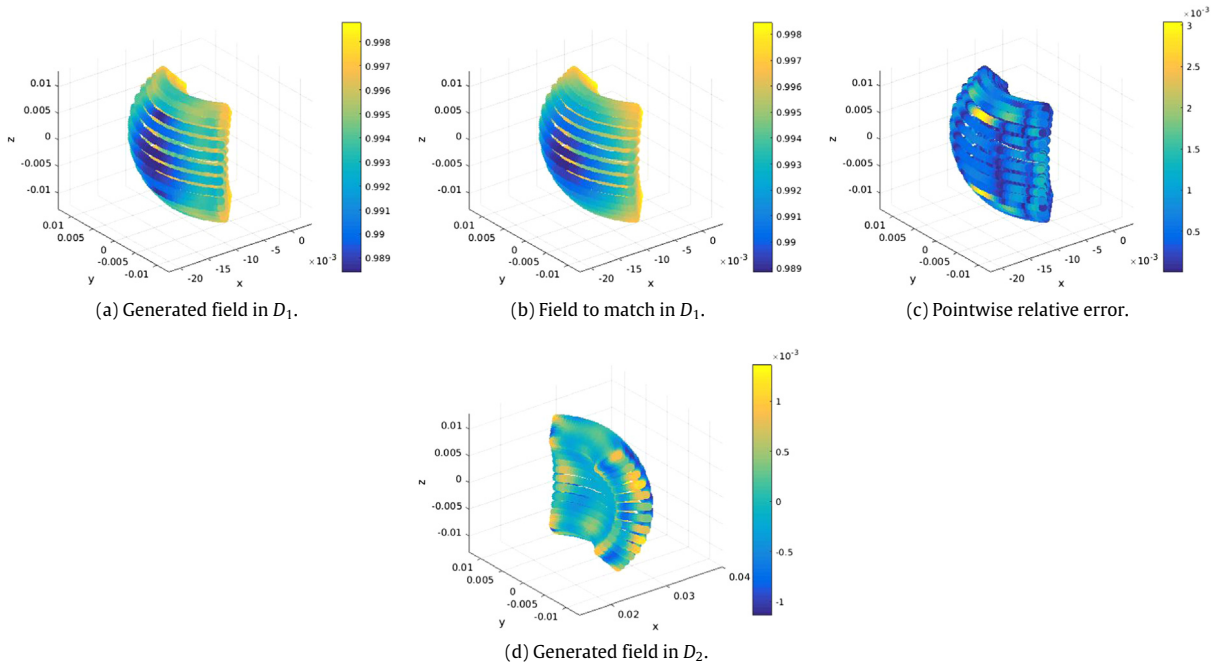


Fig. 8. Demonstration of control accuracy in D_1 and D_2 .

right plot it can be observed how the source works to approximate a plane wave corresponding to a straight black strip in region D_1 to its left while maintaining a null in region D_2 to its right. Indeed, the plots of Fig. 9 show the time propagation of the generated field by focusing on the portion of the field with amplitude approximately equal to 0.6 marked as a dark stripe. It can be observed how this portion of the field enters region D_1 at time $kct = \frac{85}{50}\pi$ in a nearly rectilinear shape and continues to keep the same form outgoing throughout a neighbourhood of region D_1 (thus indicating the plane wave structure of the approximated field in the control region) while in all the plots the field is approximately zero in region D_2 .

The time domain animation 4 [34] enhances the message of Fig. 9. The multimedia file presents the cross-sectional view along $z = 0$ of the time-harmonic evolution of the field generated by the synthesized source and respectively the propagating plane wave $u_1 = e^{-ixk}e^{-ikt}$ in a near field region given by $(x, y) \in [-0.05, 0.05]^2$ in two simultaneous animations: the top one describing the time propagation of the generated field and the bottom one describing the time propagation of the plane wave $u_1 = e^{-ixk}e^{-ikt}$. The colour scheme in the movies is (truncated to 1 light yellow and -1 dark blue) with region $D_{a'}$ removed from the simulations (coloured cyan) and with the black stripe representing

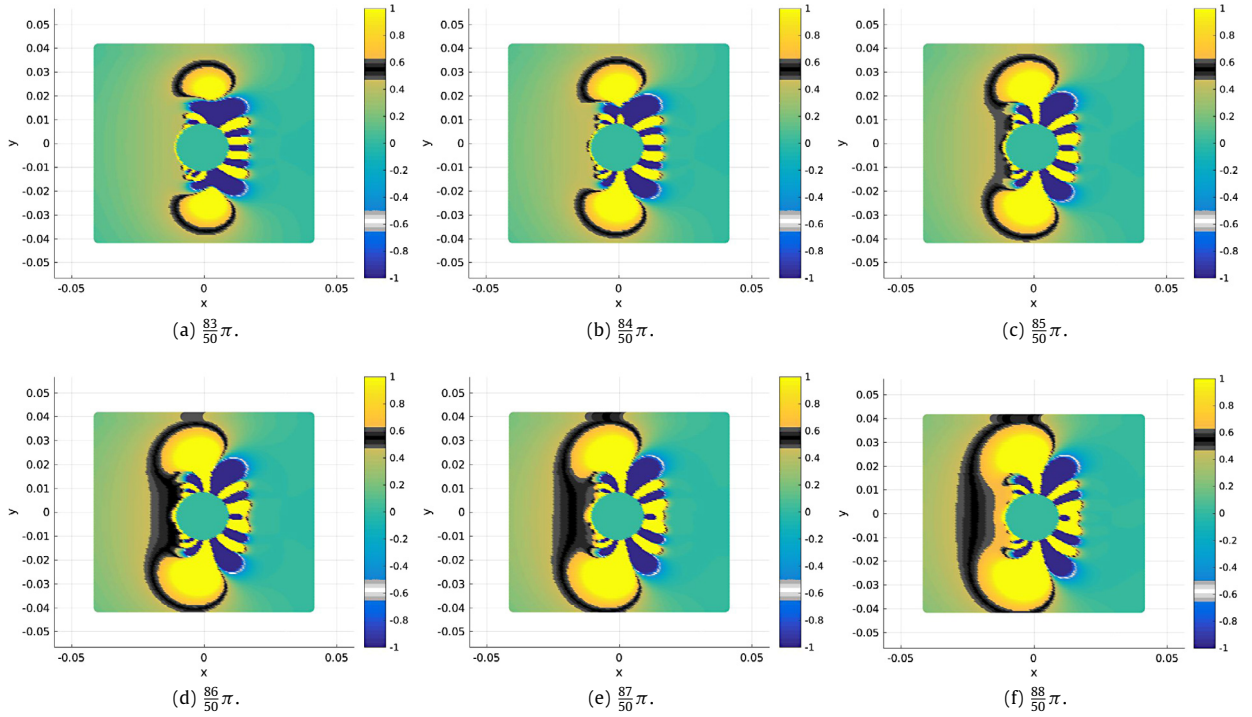


Fig. 9. Cross-sectional ($z = 0$) time snapshots of the propagating generated acoustic field for different values of kct . Control region D_1 to the left of the source, with the null region D_2 to the right. (For interpretation of the references to colour in this figure legend, the reader is referred to the web version of this article.)

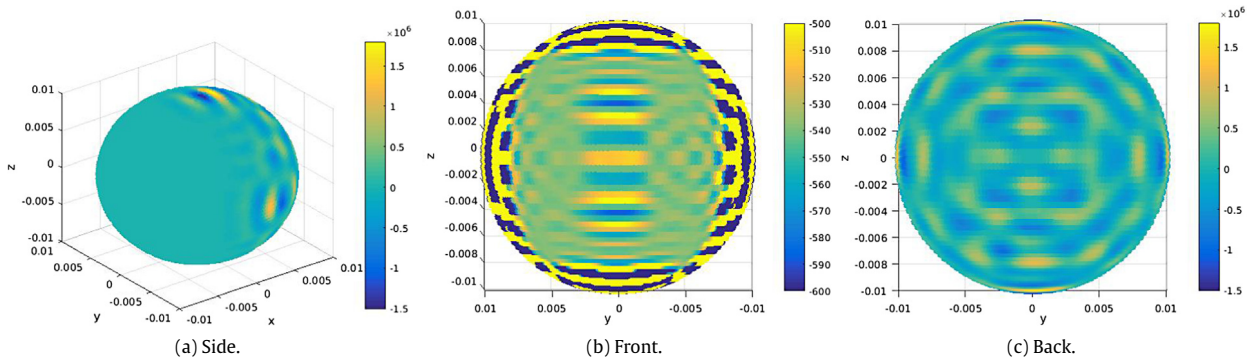


Fig. 10. Input density w_α with various colour maps highlighting the local oscillations.

amplitude values approximately equal to 0.6, and the white stripe representing amplitude values approximately equal to -0.6 respectively. As above, we point out that there are two black stripes and respectively two white stripes per period for the approximated plane wave. The animation clearly shows the accuracy of the approximation in region D_1 as well as the null in region D_2 .

Fig. 10 describes the density w_α (see (3.11)) on the boundary of the fictitious domain $D_{\alpha'}$ (recall Remark 2.1 for the location and shape of the actual physical source D_a) as an indication of the possible complexity of the required source inputs v_n or p_b described at (2.4) or (2.5). In the left plot in the figure we present the density values on the surface of $D_{\alpha'}$ viewed from a 3D side perspective and for better visualization we show two more plots in the figure; the centre plot shows the density values on the part of the surface facing region D_1 ; the right plot of the figure presents the density values on the part of the surface facing D_2 . We observe an overall larger norm of the density with larger amplitude and faster pace of the oscillations when compared with the case studied in Section 3.1 fact which is somehow not surprising due to the extra requirement that the antenna maintains a null in region D_2 .

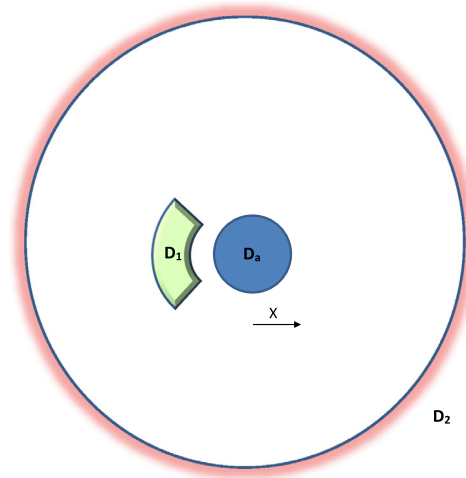


Fig. 11. Planar sketch of the geometry showing the source D_s , the control region D_1 and the far field region D_2 .

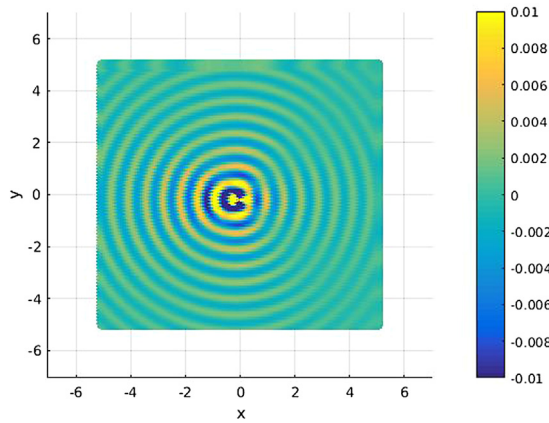


Fig. 12. Cross-section $z = 0$ plot of the generated field, showing outgoing character, with fast radiation decay.

3.3. Almost non-radiating acoustic sources with controllable near fields

In this section we present a third application of the results discussed in Section 2.1 and study the problem in the case (2.1)(iii). As an extreme example, we show how the source synthesized by our scheme approximates an incoming plane wave $u_1 = e^{ixk}$ (propagating towards the source in the positive x direction as observed from within region D_1) with wave number $k = 10$ in region D_1 (described at (3.14)) while having a very small field in region $D_2 = \mathbb{R}^3 \setminus B_{10}(\mathbf{0})$ where $B_{10}(\mathbf{0})$ denotes the ball centred at the origin with radius 10). A sketch of the geometry is presented in Fig. 11.

We mention that in this section numerical simulations region D_1 is discretized as in Section 3.1 while the far field boundary, i.e., the sphere $R = 10$, is discretized with a total of 3200 points as follows: 80 equidistant azimuthal increments by 40 equidistant polar increments respectively. Fig. 12 shows a cross-sectional view of the generated field along $z = 0$ in a region characterized by $(x, y) \in [-5, 5]^2$. This plot demonstrates the source causality (i.e., the fact that the synthesized source field is outgoing). This fact can also be observed in the time domain simulation presented in animation 5[35] where the propagating time-harmonic field generated by the synthesized source is shown.

In Fig. 13 we show the quality of our control results in region D_1 as required by (2.3). The left and centre plots in the figure describe respectively the field generated by the source u , and the plane wave to be approximated $u_1 = e^{ixk}$. The accuracy of our approximation ($O(10^{-3})$) can be observed in the right plot of Fig. 13 where the relative pointwise error between the synthesized field u and $u_1 = e^{ixk}$ is presented.

Fig. 14 shows the fast decay in region D_2 as required by (2.3). Indeed, the left plot of the figure describes the very small values of the generated field computed on the sphere of radius 10 (≈ -60 dB). On the other hand, the right plot of the figure describes the absolute values of $r \cdot \sup_{B_r(\mathbf{0})} |u|$ as a function of $r \in (10, 1000)$. The asymptotic limit of this function, $O(10^{-2})$, is the supremum value of far field pattern and this once more confirms the fact that the source synthesized by our scheme is a

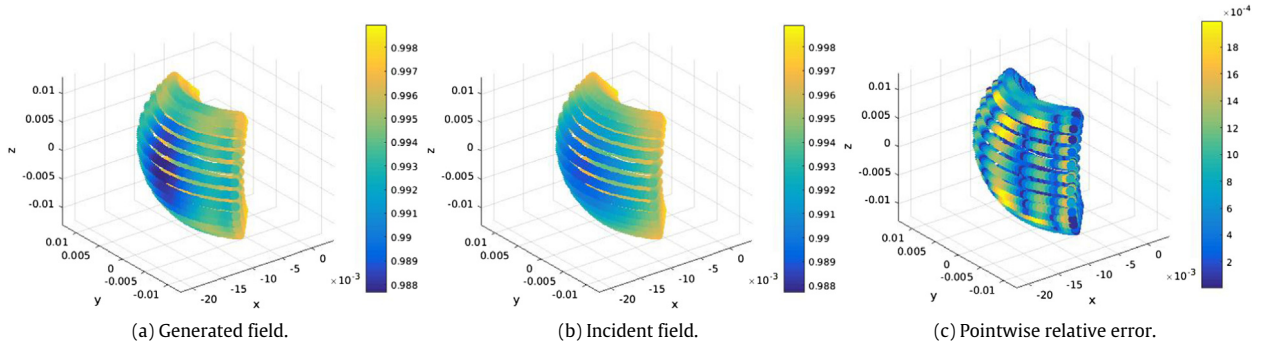


Fig. 13. Accuracy of control in region D_1 .

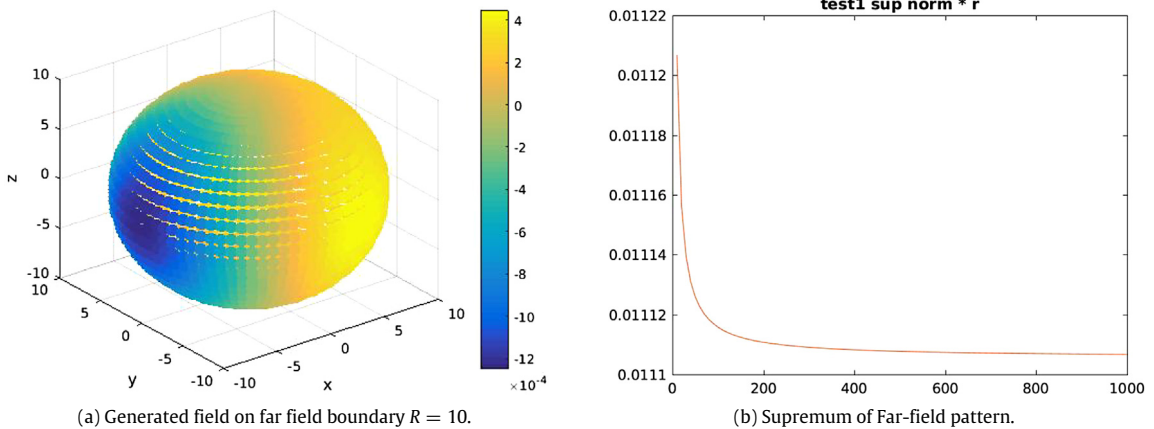


Fig. 14. Evidence of almost non-radiating character.

weak radiator. In fact, we also computed the actual power radiated by this source, i.e., $P = \text{Re}(\int_S u^* \mathbf{v} \cdot \mathbf{n})$ where u represents the pressure field solution of (2.2), (2.3), A^* denotes the complex conjugate of complex quantity A , and $\mathbf{v} \cdot \mathbf{n}$ denotes the normal velocity on a sphere S surrounding the source D_a , and we found that it is of order $O(10^{-7})$, (or -140 dB), once more indicating a very weak radiator.

Fig. 15 shows nine a cross-sectional views of the generated field along $z = 0$ in a near-field region characterized by $(x, y) \in [-0.05, 0.05]^2$. The figure describes in order left to right from top left to bottom right plot, nine cross-sectional ($z = 0$) time-snapshots ($kct = \{\frac{79}{50}\pi, \frac{80}{50}\pi, \frac{81}{50}\pi, \frac{81.5}{50}\pi, \frac{81.7}{50}\pi, \frac{82}{50}\pi, \frac{82.1}{50}\pi, \frac{83}{50}\pi, \frac{84}{50}\pi\}$) of the time-harmonic field generated by the synthesized source in the near field region. The colour scheme in the plots is (truncated to 1 light yellow and -1 dark blue) with the region $D_{a'}$ (coloured cyan) not included in the numerical simulations and with the black stripe representing field amplitudes approximately equal to 0.6.

Following the plots in order from top left to bottom right plot it can be observed how the source works to approximate the incoming plane wave $u_1 = e^{ixk}e^{-ikt}$ in D_1 . Indeed, the (a), (b) plots show how the source works on creating a plane wave in region D_1 . The (c), (d), (e), (f) plots are zoomed in closer to the antenna in a region $(x, y) \in [-0.02, 0.02]^2$ so that the approximation of the incoming plane wave is better observed. It can be seen in these plots how the portion of the fields with values approximately equal to 0.6 (black stripe) enters region D_1 at time $kct = \frac{81.5}{50}\pi$ in a nearly rectilinear shape (i.e. corresponding to plane wave character) and propagates towards the source while continuing to keep the same rectilinear form throughout the neighbourhood of region D_1 . In the last two plots we see how the generated field looses form near the source and propagates away from it in the far field (i.e., corresponding to a causal source).

The time domain animation 6 [36] presents the cross-sectional view along $z = 0$ of the time-harmonic evolution of the field generated by the synthesized source and respectively the incoming plane wave $u_1 = e^{ixk}e^{-ikt}$ in a near field region given by $(x, y) \in [-0.05, 0.05]^2$. The multimedia file shows two animations: the top one describing the time propagation of the generated field and the bottom one describing the time propagation of the plane wave $u_1 = e^{ixk}e^{-ikt}$. The colour scheme in the movies is (truncated to 1 light yellow and -1 dark blue) with the region $D_{a'}$ removed from the simulations and with the black stripe representing amplitude values approximately equal to 0.6, and the white stripe representing amplitude

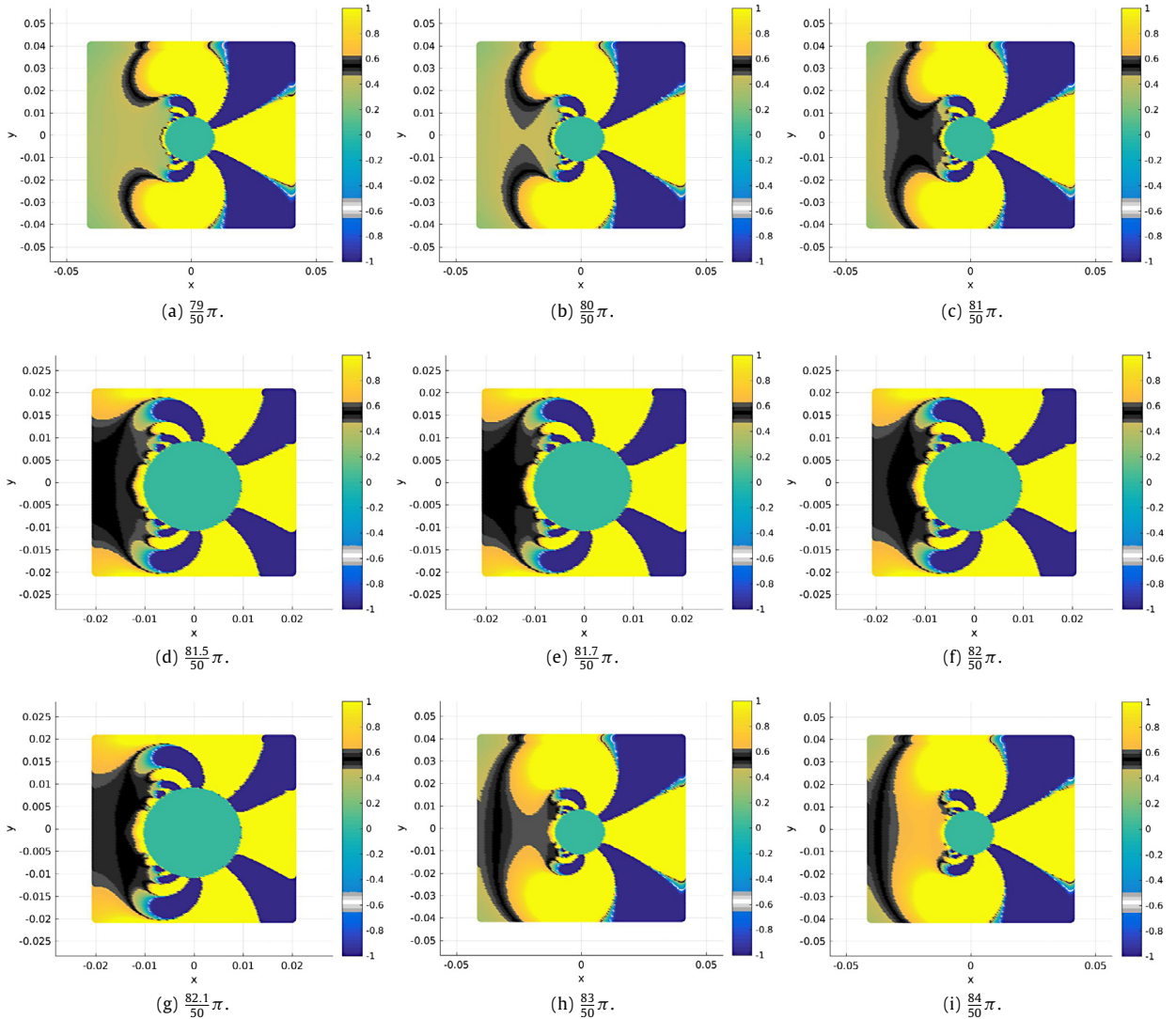


Fig. 15. Cross-sectional ($z = 0$) time snapshots of the propagating generated field for different values of kct . Control region D_1 to the left of the source, where an incoming wave is approximated. (For interpretation of the references to colour in this figure legend, the reader is referred to the web version of this article.)

values approximately equal to -0.6 respectively. As above note that there will be two black stripes and respectively two white stripes per period for the approximated plane wave. The animations show the accuracy of the approximation of the outgoing plane wave $u_1 = e^{-ixk} e^{-ikt}$ in region D_1 .

Fig. 16 shows the density w_α (see (3.11)) on the boundary of the synthesized source. In the left plot in the figure we present the density values on the surface of the source viewed from a 3D side perspective and for better visualization we show two more plots in the figure; the centre plot shows the density values on the part of the surface facing region D_1 ; the right plot of the figure presents the density values on the opposite pole of the source. We observe a large norm of w_α with complex small and respectively large scale oscillatory patterns on the two poles.

4. Conclusions and future work

In the time-harmonic regime we described a unified framework where the possibility to characterize boundary source inputs for the control of acoustic fields in homogeneous infinite media (Section 2.1) or finite depth homogeneous ocean environments (Section 2.2) was theoretically established. We then presented a 3D optimization scheme (Section 3) based on the Method of Moments and Tikhonov regularization with Morozov discrepancy principle for the numerical characterization of boundary inputs (normal velocity or pressures) necessary on the boundary of the source to obtain the

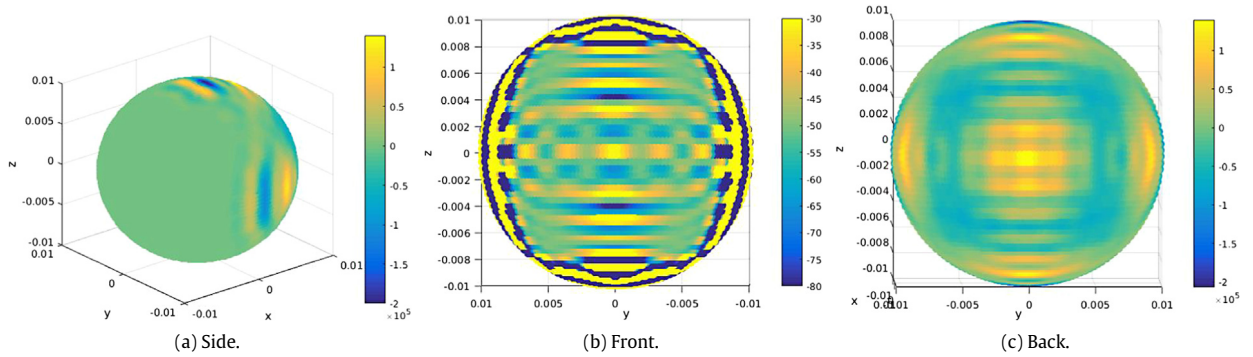


Fig. 16. Input density w_α with various colour maps highlighting the local oscillations.

desired control effects. We then numerically discussed the performance of our scheme for the problem in homogeneous infinite environments in the three distinct geometrical situations described at (2.1). We did not show any explicit numerical simulations for the case of finite depth homogeneous ocean environments but, as shown in Section 2.2, in this case the associated Green's function is computed explicitly in [26] and is a continuous perturbation of the free space Helmholtz fundamental solution, hence the optimization scheme presented in the paper can be adapted to this case as well and this will be a part of our forthcoming report.

Our work discusses a novel strategy for 3D sound field synthesis. This area of research presents a multitude of possible applications of interest to the acoustic community (see [24] section 5 for a list of possible applications). We believe that the results presented in this report may be in particular relevant to:

1. Strategies for synthesis of virtual sound fields or for acoustic focusing (Section 3.1). Indeed, the numerical observations suggest that the results of Section 3.1 hold true for control regions D_1 located in the near field of the source D_a with the condition that ka' is larger than a give threshold. In this context the synthesis of virtual arbitrary sound fields in region D_1 becomes possible through a Fourier synthesis procedure and we could imagine an application where a single source or an array of such sources will be synthesized to approximate a focused signal in a region D_1 (exterior to the array or interior to the convex hull of the array).

2. Strategies for generating personal audio spots, null placement or covert communications (Section 3.2); Indeed, we performed a sensitivity analysis for the case considered in Section 3.2 and discovered that in principle (with associated increases in source input complexity) the results remain valid for various locations of the null region D_2 relative to region D_1 even in the case when the are coaxial both centred on the negative x axis for example. This together with a superposition principle indicate the possibility to characterize single sources or arrays to generate personalized sound signals in disjoint exterior regions, or obtain desired null regions or approximate a given signal in a region while maintaining a null in another prescribed area thus achieving a covert communication with respect to the null region. For example, another way to imagine a covert communication device is by noting that the theoretical results presented in [21] imply the possibility to create almost non-radiating sources which are approximating any desired acoustic field in sub-region D_1 . In fact our numerics suggest that the case presented in Section 3.3 is an extreme example where the signal to be approximated in region D_1 is propagating towards the source and other outgoing signals will be much easier to approximate. In this context, one can imagine an almost non-radiating array which is thus covertly transmitting in region D_1 a desired prescribed signal.

3. Strategies for acoustic protection from active interrogation. In this setup, one envisions a planar array in front of (or a conformal array surrounding) the protected area paired with exterior sensors for the detection of interrogating signals (through an associated time control feedback loop). The array (planar or conformal) of source elements similar to the element described in Section 3.3 is then synthesized (through appropriate Fourier synthesis) as a very weak radiator (thus unobservable to a far field measurement device) with a controllable near-field such that it nulls (by destructive interference) an interrogating field thus creating a protected shadow region behind (the case of planar array), or a protected region within the convex hull (the case of conformal array).

4. Strategies for acoustic noise cancellation. Indeed we can imagine a conformal array of elements surrounding (at some distance) a noise source and where each element in the array is attached to a sensor located in the interior of the elements convex hull. Using a Fourier synthesis procedure and based on our theoretical results [21] this array can be synthesized to generate a null in an interior region containing the sensors (thus guaranteeing accurate measurements) while (using feed forward information from the sensors about the signal to be cancelled) the total field exterior to the array convex hull can be made vanishingly small.

As pointed out before, our preliminary numerical investigations show that, assuming more harmonics in the expansion of the density w_α we could achieve the same degree of control with the near field regions D_1 and D_2 located further away from the source (giving thus more freedom in the choice of an actual physical boundary ∂D_a) or when one considers more than two regions of control. In this regard, in the spirit of [23], a detailed study of the sensitivity of the optimization scheme

with respect to parameters such as, relative position of the control regions D_1 and D_2 and their distance from the source D_a , power budget and oscillatory character of the source input as well as acoustic intensity of the source is currently undergoing and will be presented in future reports.

The study of arrays where one considers coupling effects as well as realistic possibilities for the instantiation of the theoretically predicted inputs is also an important part of our future research programme

Additionally, we observed throughout our numerical simulations (see Figs. 5, 10 and 16) that the synthesized source may require a very complex input on its boundary with possibly large amplitude, i.e., with sub-areas characterized by small values and fast oscillations (e.g., the part facing D_1) and other sub-areas characterized by very large values and slower oscillations (e.g., the pole opposite to D_1).

In the context of linear approximation where everything can be scaled down appropriately, the results presented above in Figs. 8, 10, 13 and 16 corroborated with the superposition principle suggest the possibility of approximating arbitrary given patterns (with small amplitudes) in each of the regions of interest. We also remark that the high possible norm of the L^2 boundary input can be mitigated by considering arrays of such elements in achieving the desired control effect.

On the other hand, the undesirable small scale and large scale fast oscillations observed at the above L^2 solution could be addressed by allowing the regularization parameter to be smaller or by considering different penalties (other than $\|w\|_{L^2(\partial D_a)}$) in the Tikhonov regularization discrepancy functional defined at (3.12) such as, the total variation norm of the velocity (or pressure) ((2.4) or (2.5) for free space and (2.9) or (2.10) for homogeneous ocean environments respectively).

Last but not least, we believe that by using a Fourier synthesis technique our strategy can be extended to the time-domain synthesis of band-limited signals where different prescribed signals could in principle be synthesized in disjoint near field regions. This, and, if needed, a direct time-domain analysis will be another important part of our future work.

Acknowledgements

This work was supported by the Office of Naval Research under the award N00014-15-1-2462 and Daniel Onofrei would also like to thank the Institute for Mathematics and its Applications (IMA) for the generous support during the fall semester of 2016 when a part of this work was finalized.

Appendix A. Supplementary data

Supplementary material related to this article can be found online at <https://doi.org/10.1016/j.wavemoti.2017.10.004>.

References

- [1] C.R. Fuller, A.H. von Flotow, Active control of sound and vibration, IEEE (1995).
- [2] N. Peake, D.G. Crighton, Active control of sound, *Annu. Rev. Fluid Mech.* 32 (2000) 137–164.
- [3] P. Nelson, S.J. Elliott, Active Control of Sound, Academic, London, 1992, p. 436.
- [4] H.F. Olson, E.G. May, Electronic sound absorber, *J. Acad. Soc. Am.* 25 (1953) 1130–1136.
- [5] P. Leug, Process of silencing sound oscillations, U.S. patent no. 2043416, 1936.
- [6] Y.H. Kim, J.W. Choi, Sound field reproduction, in: *Sound Visualization and Manipulation*, Wiley, Singapore, 2013, pp. 283–370.
- [7] R. Rabenstein, S. Spors, Sound field reproduction, in: *Springer Handbook of Speech Processing*, Springer-Verlag, Berlin, Heidelberg, 2008, pp. 1095–1114.
- [8] M.A. Poletti, F.M. Fazi, An approach to generating two zones of silence with application to personal sound systems, *J. Acoust. Soc. Am.* 137 (2015) 598–605.
- [9] S.J. Elliott, J. Cheer, H. Murfet, K.R. Holland, Minimally radiating sources for personal audio, *J. Acoust. Soc. Am.* 128 (2010) 1721–1728.
- [10] J. Cheer, S.J. Elliott, M.F.S. Galvez, Design and implementation of a car cabin personal audio system, *J. Audio Eng. Soc.* 61 (2013) 412–424.
- [11] P. Coleman, P.J. Jackson, M. Olik, J.A. Pedersen, Personal audio with a planar bright zone, *J. Acoust. Soc. Am.* 136 (2014) 1725–1735.
- [12] E. Friot, C. Bordier, Real-time active suppression of scattered acoustic radiation, *J. Sound Vib.* 278 (2004) 563–580.
- [13] J. Loncaric, V.S. Ryaben'kii, S.V. Tsynkov, Active shielding and control of environmental noise, Technical Report, NASA/CR-2000-209862, ICASE Report No. 2000-9, 2000.
- [14] J. Loncaric, S.V. Tsynkov, Quadratic optimization in the problems of active control of sound, *Appl. Num. Math.* 52 (2005) 381–400.
- [15] D.A.B. Miller, On perfect cloaking, *Opt. Express* 14 (2006) 12457–12466.
- [16] F.G. Vasquez, G.W. Milton, D. Onofrei, Active exterior cloaking, *Phys. Rev. Lett.* 103 (2009).
- [17] F.G. Vasquez, G.W. Milton, D. Onofrei, Broadband exterior cloaking, *Opt. Express* 17 (2009) 14800–14805.
- [18] F.G. Vasquez, G.W. Milton, D. Onofrei, Exterior cloaking with active sources in two dimensional acoustics, *Wave Motion* 48 (6) (2011) 515–524.
- [19] A.N. Norris, F.A. Amirkulova, W.J. Parnell, Source amplitudes for active exterior cloaking, *Inverse Problems* 28 (10) (2012).
- [20] J. Cheer, Active control of scattered acoustic fields: Cancellation, reproduction and cloaking, *J. Acoust. Soc. Am.* 140 (2016) 1502.
- [21] D. Onofrei, Active manipulation of fields modeled by the helmholtz equation, *J. Acoust. Soc. Am.* 26 (4) (2014) 553–579.
- [22] D. Onofrei, On the active manipulation of fields and applications. I - The quasistatic regime, *Inverse Problems* 28 (10) (2012).
- [23] M. Hubenthal, D. Onofrei, Sensitivity analysis for active control of the Helmholtz equation, *Appl. Numer. Math.* 106 (2016) 1–23.
- [24] J. Ahrens, Analytic methods of sound field synthesis, in: *T-Labs Series in Telecommunications Services*, Springer, 2012.
- [25] J.B. Keller, J. S. Papadakis, Wave propagation and underwater acoustics, in: *Lecture Notes in Physics*, Springer-Verlag, Berlin, 1977.
- [26] J. Buchanan, R. Gilbert, A. Wirgin, Y. Xu, Marine acoustics, *Direct Inverse Probl. SIAM* (2004).
- [27] D. Colton, R. Kress, Integral equation methods in scattering theory, *SIAM Ser.: Class. Appl. Math.* 72 (2013).
- [28] T. Arens, D. Gintides, A. Lechleiter, Variational formulations for scattering in a three-dimensional acoustic waveguide, *Math. Methods Appl. Sci.* 31 (7) (2008) 821–847.
- [29] A. Bakushinsky, A. Goncharsky, Ill-Posed Problems: Theory and Applications, Kluwer Academic Publishers, Denmark, 1994.
- [30] H.W. Engl, M. Hanke, A. Neubauer, Regularization of inverse problems, in: *Math. Appl.*, Kluwer Academic Publishers, Springer, New York, 1975.

- [31] <https://drive.google.com/open?id=0B7nf-pdU3Z4DZkIDRGpfWEtEWIU>, Accessed: 2017-09-09.
- [32] <https://drive.google.com/open?id=0B7nf-pdU3Z4DNGRhMEVMSTF5UFE>, Accessed: 2017-09-09.
- [33] <https://drive.google.com/open?id=0B7nf-pdU3Z4DaHJmOHhjWjh2SVE>, Accessed: 2017-09-09.
- [34] <https://drive.google.com/open?id=0B7nf-pdU3Z4DOFk5NW9OX3FEUuk>, Accessed: 2017-09-09.
- [35] <https://drive.google.com/open?id=0B7nf-pdU3Z4DZVliOHZIVXFobXM>, Accessed: 2017-09-09.
- [36] <https://drive.google.com/open?id=0B7nf-pdU3Z4DNjBjaHBqRTjpVDQ>, Accessed: 2017-09-09.